Computation of heat transfer in a linear turbine cascade

By Georgi Kalitzin & Gianluca Iaccarino

1. Motivation and objectives

The efficiency of a turbine increases in general with an increase of the temperature of the working gas. In modern turbines this gas temperature may well exceed the melting temperature of the metal walls (Harasgama, 1995). Locally high heat transfer can lead to an excessive temperature and high thermal stresses in the walls, causing an early fatigue of the high pressure turbine components. Thus, the design of these components requires accurate evaluation of heat transfer at the walls.

The prediction of heat transfer at the endwall and the blade surface requires simulation of the viscous interaction between the boundary layer approaching the blade and that developing on the blade itself. Secondary flows, horseshoe type vortices, and strong turbulence effects generate complex endwall heat transfer distributions with several local maxima occurring at the endwall and the blade surface. Accurate prediction of these peaks is crucial for the design of the turbine cooling system.

Recently, a detailed experimental investigation of the endwall heat transfer in a linear cascade was carried out at the NASA Glenn Transonic Turbine Blade Cascade Facility. This investigation includes the effects of Mach and Reynolds number and the influence of the free stream turbulence on the endwall and blade surface heat transfer rate. A large database has been created through this work for the validation of numerical methods for the simulation of turbine flows.

The objective of the present work is to use this database to evaluate the influence of turbulence models on the accuracy of heat transfer predictions in complex three-dimensional flows in turbine geometries. The sensitivity of the heat transfer coefficient prediction to the turbulence model used is analyzed using two different models: the Spalart-Allmaras one equation model (Spalart & Allmaras 1992) and Durbin's four equation v^2-f model (Durbin 1995). The use of two different flow solvers, the NASA research code CFL3D and the commercial package FLUENT, increases confidence in the results and allows the elimination of effects related to the numerical discretization of the equations.

2. Accomplishments

2.1 Numerical method

The present results have been computed using two different RANS flow solvers: the NASA code CFL3D and the commercial software FLUENT 5.

CFL3D (Krist *et al.* 1998) is a compressible, finite-volume code for multi-block structured grids. The mean flow fluxes are computed with the Roe flux difference splitting scheme. Turbulence models are solved segregated from the mean flow in an

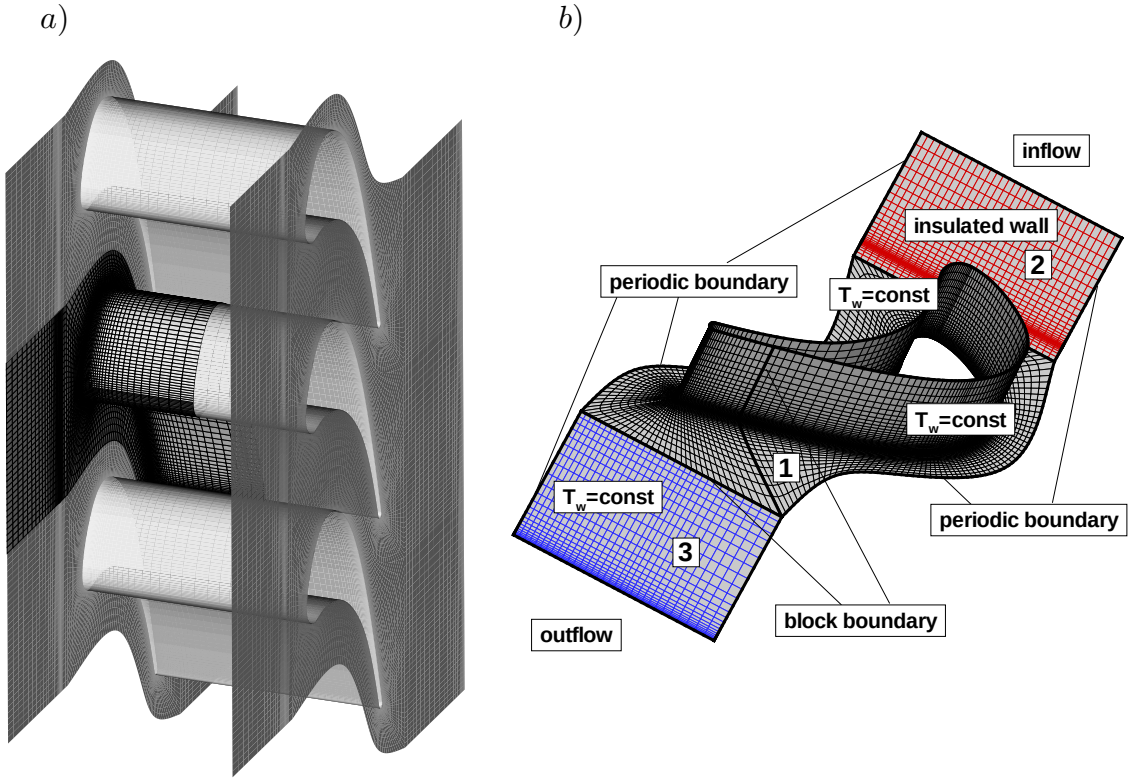

FIGURE 1. Sketch of linear turbine cascade and computational domain.

implicit manner using three-factored Approximate Factorization. The v^2-f model has been implemented in this code in an implicit pairwise coupled manner with an implicit treatment of the boundary conditions. The resulting linear algebraic system is solved with a three- or two-factored Approximate Factorization scheme (Kalitzin 1999).

FLUENT (version 5) is a commercial CFD package developed by Fluent Incorporated (FLUENT 5, 1998). It solves the time-dependent RANS equations on structured and unstructured meshes using a control-volume-based technique; the diffusion terms are discretized using a second-order central-difference scheme while a second-order upwind scheme is employed for the convective terms. An Euler implicit discretization in time is used in combination with a Newton-type linearization of the fluxes. The resulting linear system is solved using a point Gauss-Seidel scheme in conjunction with an algebraic multigrid method. The additional equations for the turbulent quantities are solved in a segregated fashion using a first- or second-order upwind discretization scheme with explicit boundary conditions.

2.2 NASA transonic cascade

The large scale linear cascade investigated in the experiments (Giel *et al.* 1998, 1999) consists of twelve blades with an axial chord of 12.7 cm. A part of the cascade is shown in Fig. 1a. The high blade count of the cascade ensures good periodicity. This allows us to consider only one blade and only the region between endwall and symmetry plane in the computations. The actual computational domain is shown in Fig. 1b. The block boundaries of the structured 3-block mesh and the boundary

conditions used are highlighted in the figure.

An O-mesh topology around the blade has been chosen to ensure a high quality mesh near the blade surface. The two-dimensional mesh consisting of 48x192 cells has been generated through simple geometric interpolation. After generating the outer boundary as an arbitrary line between two blades and distributing lines connecting the outer boundary with the blade, O-lines have been interpolated using a stretching function. Normality between the grid lines and the blade surface has been ensured by interpolating the angle between the grid lines, enforcing 90 degrees at the surface. The coordinates of a grid point have been adjusted with a smoothing function using the coordinates of the neighboring points on an O-line. Special attention has been paid to ensure a one-to-one connectivity on the periodic boundaries. An additional block with 32×32 cells at the inflow and a block with 24×32 cells at the outflow have been attached to locate the inflow boundary at 1 cord length upstream of the leading edge and the outflow boundary at 1.2 cord length downstream of the trailing edge.

The three-dimensional mesh has been generated by copying the described 2-D grid in the spanwise direction and clustering the grid points at the endwall. Two meshes, mesh A and mesh B, have been generated with 40 and 52 cells spanwise, respectively. All block dimensions have been chosen to contain factors of the power 2 to exploit multigrid. The mesh has been transformed into an unstructured mesh for the flow computations with FLUENT. The multiblock decomposition disappears for an unstructured solver. The height of the first cell above the wall has an average y^+ value of about 1. The height has been adjusted after initial computations.

The mesh described above differs from the one used in Kalitzin & Iaccarino (1999) mainly in the clustering of cells at 0.3 cord length upstream of the blade. The wall boundary condition for the energy equation changes here from an insulated wall to a constant wall temperature. The mesh A has the same spanwise distribution as in the previous work. Mesh B, however, has not only more cells spanwise, but they have been distributed more towards the symmetry plane. The effect of this is described in section 2.5.

The experimental data are provided for a set of exit Mach number and inlet Reynolds number with and without grids for generating turbulence at the inlet. The case with an inlet Mach number of 0.38, an exit Mach number of 1.33, and an inlet Reynolds number of 937,000 has been selected for the present investigation. The flow incidence is 63.64^o. The cascade provides a design flow turning of 136^o. The pressure ratio p_i/p_e used in the computation is 0.37. The inlet profile is modeled as a thick boundary layer with $\delta_i/C_x = 0.24$. Periodic boundary conditions are imposed on the boundaries between the blades. The computations have been carried out with a constant wall temperature T_w of $450K$.

2.4 Two-dimensional results

In the simulation of three-dimensional flow, the computational grid is often a compromise between a desired resolution and computational affordability. In two dimensions, however, it is easier to carry out a complete grid sensitivity study. With this objective in mind, the flow in the symmetry plane has been computed in

a two-dimensional plane.

The structured grid, or default mesh, for this report is shown in Fig. 2a. It is the same used at each spanwise location in the three-dimensional calculations. It contains 11008 cells. The unstructured grid, shown in Fig. 2b, is obtained through successive refinement in regions with high pressure gradients and large strain rates like shock waves, boundary layers, and wakes. This mesh contains 71326 cells.

The Mach contours plotted for both grids show a very complex shock wave pattern in the wake of the blades. The accelerating flow within the passage generates an oblique shock wave on the pressure side of a blade. This shock is reflected on the suction side of the successive blade. It then interacts with the viscous wake of the blade from which it originated. A second shock wave is generated on the suction side near the trailing edge. The default mesh does not resolve the shock waves in the wake. Only the two shocks at the trailing edge are clearly visible.

The Stanton number distribution on the blade for both grids is shown in Fig. 3. In spite of the different wake developments, the heat transfer is in close agreement on both grids. Small differences occur only where the shock wake reflects on the suction surface. The lift and drag computed on the default and refined grid is $C_L = 3.372$, $C_D = 5.889$ and $C_L = 3.376$, $C_D = 5.892$, respectively. This may indicate that the default grid has a suitable grid resolution.

Results obtained with CFL3D are also reported in Fig. 3. Both codes are in good agreement despite the different numerical schemes used.

The heat transfer at the wall depends significantly on the thermal conductivity of the fluid. The effect of using a constant thermal conductivity at reference temperature is demonstrated with the FLUENT results reported in the same figure. The overall Stanton number is underpredicted. This explains the difference observed between the FLUENT and CFL3D Stanton number distributions at the endwall reported in Kalitzin & Iaccarino (1999). It has to be noted that the constant thermal conductivity is the default option in FLUENT.

2.5 Three-dimensional results

The pressure distributions on blade and endwall are not very sensitive to the grid resolution and inflow profile for the case considered. Both flow solvers predicted a reasonable agreement with the experiment as reported in (Kalitzin & Iaccarino, 1999). We note, however, that the pressure distribution on the blade and the shock structure is sensitive to the treatment of the periodic boundary since it is located relatively close to the blade surface. In this paper we will focus primarily on the analysis of the heat transfer distribution, on the dependence of the Stanton number distribution on inflow profile and grid resolution. The Stanton number is computed according to the definition used by Giel in experiments (Giel *et al.* 1998).

The experimental data for the endwall show some interesting features that will help to differentiate the predictive capabilities of the models tested (Fig. 6). The horseshoe vortex generated by the rolling up of the incoming boundary layer enhances the wall heat transfer, and its structure is clearly visible in the higher Stanton number (Region A). A second distinct heat transfer peak is measured near the stagnation point (Region A). Within the passage, four additional interesting features are

a) default mesh *b*) refined mesh

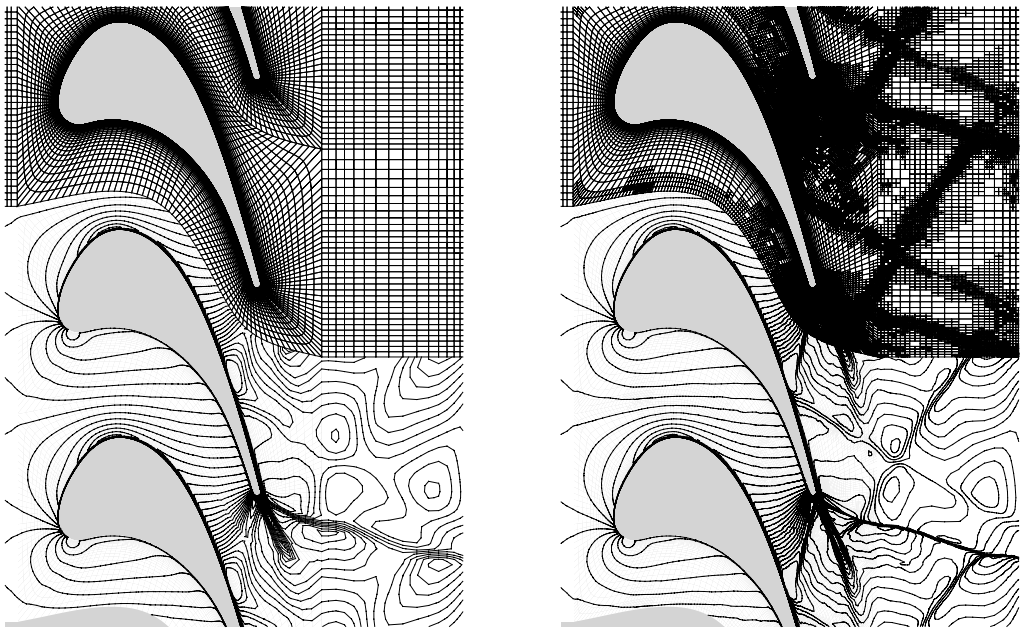

FIGURE 2. 2D grid refinement study with FLUENT; Isomach contours with $M_{min} = 0.1$, $M_{max} = 1.6$ and $\Delta M = 0.05$.

present: the first is a localized peak in the Stanton number related to the impingement of the suction-side leg of the horseshoe vortex on the blade surface (Region B). The second feature is the presence of a shock wave on the pressure side near the the trailing edge that increases the heat transfer on the endwall (Region C). Third, there is a gradual increase of heat transfer at the endwall which is related to the acceleration of the fluid in the passage (Region D). And finally, the presence of a corner vortex on the suction side of the blade (Region E) is indicated in experiments by a low heat transfer region. In the wake, a very sharp peak in the Stanton number is measured just downstream of the trailing edge (Region C).

The numerical predictions of the Stanton number show most of the features observed in the experiments but, in general, fail to predict the quantitative heat transfer on the endwall correctly.

The increased heat transfer beneath the horseshoe vortex is captured by both turbulence models. The S-A model seems to spread this high Stanton number region and shift it towards the suction side. Spreading of the horseshoe vortex is related to the turbulence generation in the vortex shear layer. The v^2-f model tends to produce a thinner vortex. The secondary peak on the suction side (Region B), which is related to the stagnation of high temperature fluid convected by the horseshoe vortex, is predicted by both models. The v^2-f model predicts a higher value for the Stanton number. The SA model predicts slightly larger values for the gradual increase in heat transfer within the passage (Region D). The trailing edge

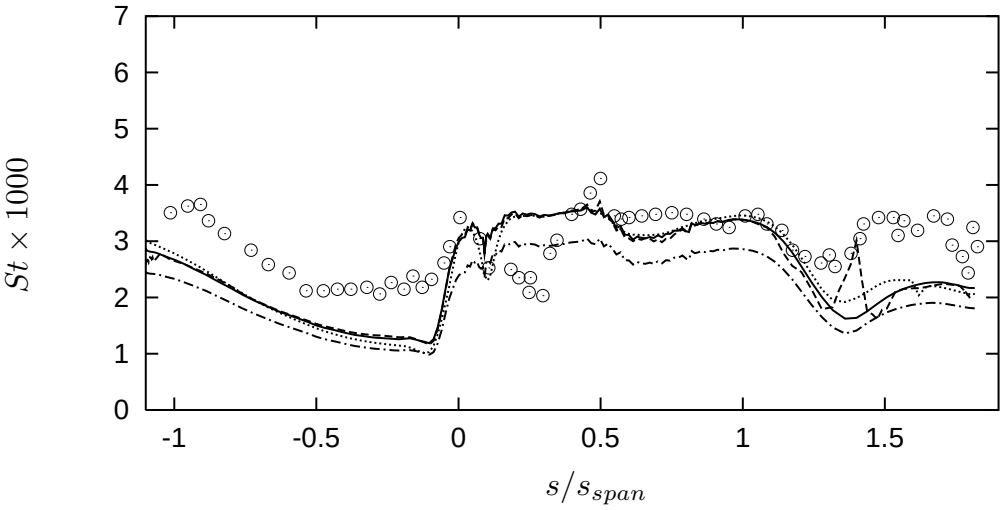

FIGURE 3. 2D grid: Stanton number distribution on blade surface; SA model; ——— : FLUENT; - - - - : FLUENT, refined mesh; —-— : FLUENT + constant thermal conductivity, ····· : CFL3D, ∘ : Exp. (3D, $y/span = 50\%$).

peak (Region C) and the low heat transfer region on the suction side of the blade (Region E) are reproduced by both models.

A quantitative comparison of the heat transfer on the blade surface is shown for three stations in Figs. 4 and 5 for the v^2-f and SA model, respectively. The experimental data set was not available in electronic form and has been scanned from Giel *et al.* (1999). The heat transfer in the stagnation region in the figure, the location where s/s_{span} is 0, is accurately predicted by both models at 25% and 50% span (solid line). Both stations are located outside of the incoming boundary layer specified at the inlet. The station at 10% span, however, is located well inside of this boundary layer, and both models overpredict the heat transfer here by 25%. The higher heat transfer indicates that the turbulence intensity is too high at this location. This observation is supported by a computation in which the turbulence levels inside the endwall boundary layer have been reduced by setting the turbulence quantities at the inlet to a uniform value corresponding to 0.25% turbulent intensity (dotted line). This lowers the Stanton number in the stagnation region to the value measured in the experiments. In addition, it delays the transition on the upper surface of the blade. The SA model shows a large sensitivity to the reduced boundary layer turbulence across the entire span on the pressure side.

The heat transfer on the pressure side of the blade is consistently underpredicted at each station by both models. The same has been observed for the 2D computation shown in Fig. 3. At this stage it is not clear whether this is due to the specification of the inlet conditions or the turbulence model.

The correct transition prediction is very important for the flow condition considered. The SA model transitions right away on the suction surface of the blade while the rise in the Stanton number is delayed with the v^2-f. It has to be noted that the SA implementation in CFL3D is lacking the transition trip functions which can be

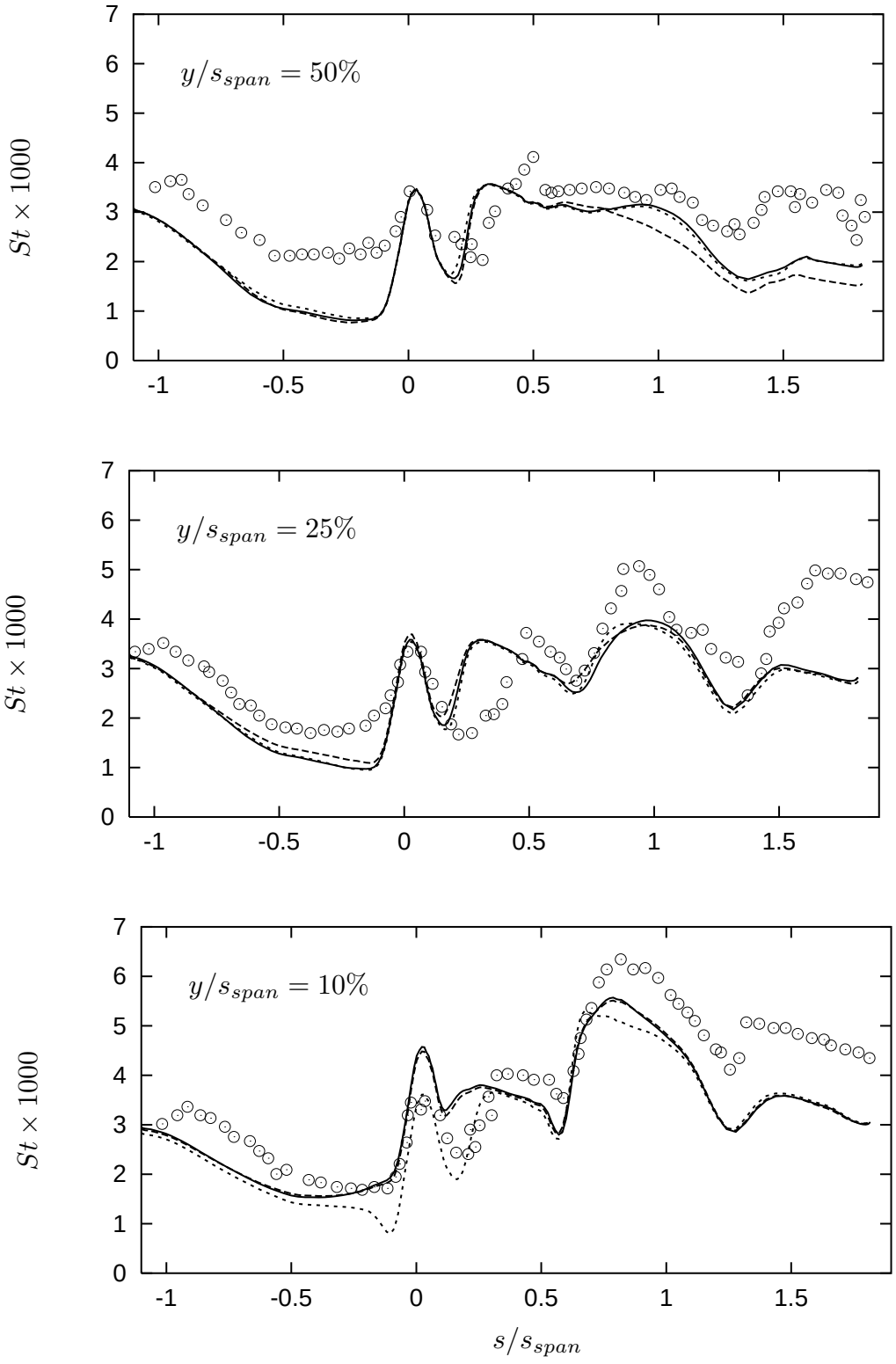

FIGURE 4. Stanton number distribution on blade surface; CFL3D; v^2-f model; ——— : mesh B and – – – – : mesh A with turbulent boundary layer at inlet, ····· : mesh B with 0.25% turbulent intensity over entire inlet, ∘ : Exp.

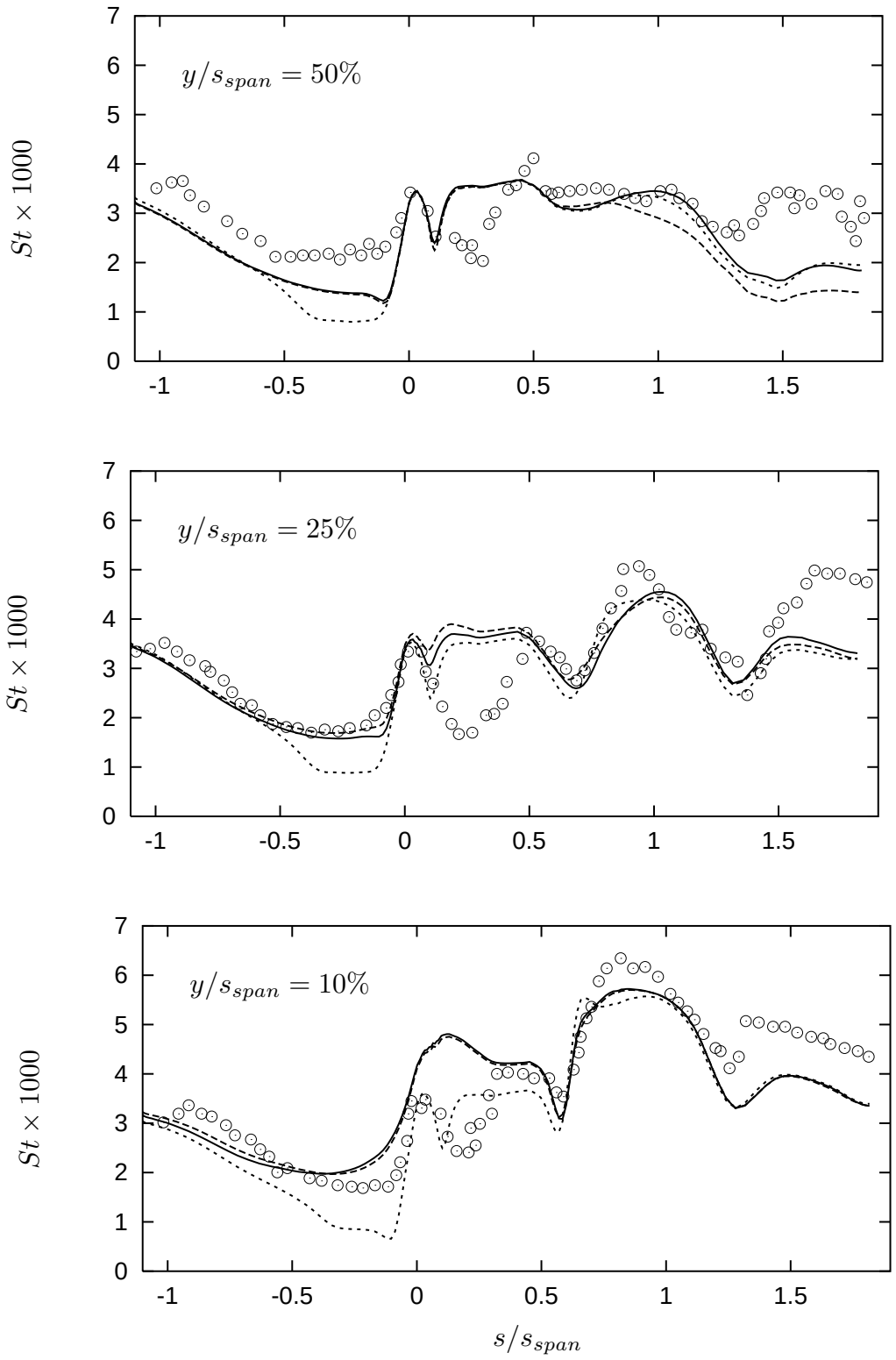

FIGURE 5. Stanton number distribution on blade surface; CFL3D; SA model; ——— : mesh B and – – – – : mesh A with turbulent boundary layer at inlet, ····· : mesh B with 0.25% turbulent intensity over entire inlet, ∘ : Exp.

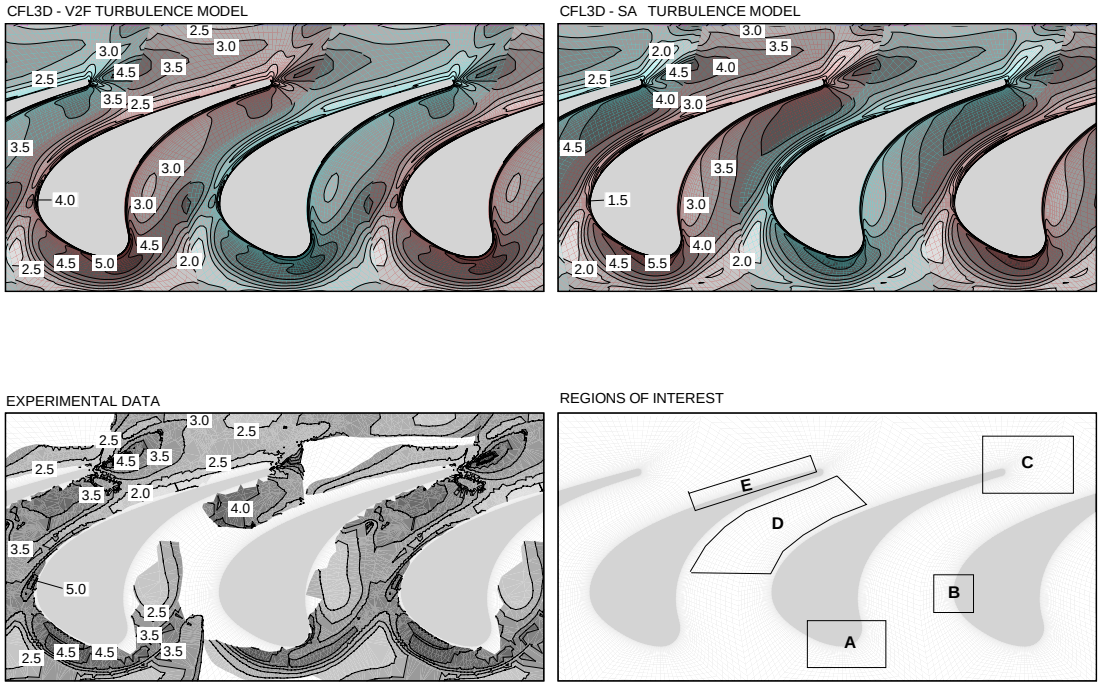

FIGURE 6. Stanton number distribution on endwall

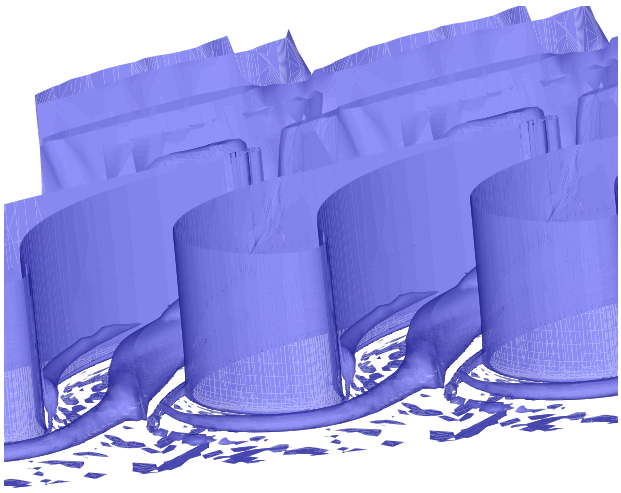

FIGURE 7. Detection of the horseshoe vortex using the method of Jeong & Hussain.

used to delay transition.

The flow in the turbine passage is strongly three-dimensional: highly turbulent flow close to the endwall is convected by the horseshoe vortex towards the middle of the blade, generating an intense cross-flow. According to the symmetry boundary condition, this flow must vanish at the middle of the blade. This requires a high spanwise resolution to capture the resulting velocity gradients. Thus the increase in the spanwise mesh resolution decreases the wall influence on the flow in the symmetry plane. The Stanton number distribution at $y/s_{span} = 50\%$ becomes similar to that in the 2-D flow computation (dashed line). Noticeable here is the Stanton number increase at $s/s_{span} = 1$ for the computation on mesh B.

The three-dimensional computations with the v^2-f model have an important numerical aspect for the multiblock computation with CFL3D. The two-factored scheme (Kalitzin, 1999) used in a computational plane with grid lines originating from the endwall and the blade surface emphasizes the efficiency of this algorithm. It also demonstrates that the multiblock concept can be used for the f-equation in three-dimensional computations.

2.6 Visualization of the horseshoe vortex

The heat transfer at the wall is increased in regions where vortices are located close to the wall, increasing the convective mixing of the fluid. Thus, information about the location of the vortices can be very important for designing turbomachinery cooling devices.

The method of Jeong & Hussain (1995) has been used here to visualize vortices. The method is based on the eigenvalues of the symmetric tensor $S^2 + \Omega^2$, where S and Ω are respectively the symmetric and antisymmetric parts of the velocity gradient tensor. A vortex is defined to be the connected region with two negative eigenvalues of $S^2 + \Omega^2$. This definition is equivalent to the requirement that the second eigenvalue λ_2 is negative inside a vortex.

The surface where λ_2 is zero is plotted in Fig. 7. The presence of a horseshoe vortex at the leading edge of the blade is clearly shown. In addition, it is possible to trace the two legs of the vortex in their development within the passage. It is worth noting that simpler vortex description methods, like detections of regions where the pressure has a minimum, do not work in this case due to the very large pressure gradient in the passage. A drawback of the present method is that boundary layers are detected as vortices as well.

3. Future plans

During the present work several factors were identified as being responsible for the scatter between numerical predictions of the heat transfer and experimental data. Among these are: the spanwise resolution of the grid, the accuracy of the numerical procedure, the specification of the inlet profiles, and the modeling of transition.

Transition modeling has a major impact on the results predicted for the flow conditions considered. Since turbulence models do not generally represent transition accurately, it is an advantage for the evaluation of turbulence models to concentrate

on those flow conditions for which the turbulence intensity at the inlet has been increased with a turbulence grid. Such data are available in Giel's papers.

Future work will concentrate on mesh resolution issues, discretization issues, and flow conditions. Preliminary results show that the discretization accuracy of the convective terms does affect the heat transfer at the endwall. The cross section of the main horseshoe vortex is represented by 4 to 6 cells and is not enough for a mesh independent representation. The effect of a finer spanwise resolution has been demonstrated for computations on mesh A and B. The grid refinement study in a two-dimensional computation indicates that the sharp resolution of the shocks in the wake is not necessary for accurate heat transfer computations on the blade. However, this may not be the case in three-dimensional computations. At this stage it is not clear how much finer the three-dimensional mesh has to be to obtain truly mesh independent solutions.

Acknowledgments

The basic algorithm for generating the two dimensional O-mesh around the blade has been written by P. Durbin. The authors also acknowledge P. Giel for providing the experimental data.

REFERENCES

Durbin, P. 1995 Separated flow computations with the $k-\epsilon-\overline{v^2}$ model. *AIAA J.* **33,** 659-664.

Fluent 5 1998 User's Guide.

Giel, P. W., Van Fossen, G. J., Boyle, R. J., Thurman, D. R., & Civinskas, K. C. 1999 Blade heat transfer measurements and predictions in a transonic turbine cascade. *99-GT-125, ASME-IGTI International Gas Turbine Conference.*

Giel, P. W., Thurman, D. R., Van Fossen, G. J., Hippensteele, A. A. & Boyel, R. J. 1998 Endwall heat transfer measurements in a transonic turbine cascade. *ASME J. Turbomachinery.*

Harasgama, S. P. 1995 Aero-thermal aspects of gas turbine flows. *Von Karman Institute Lecture Series: "Heat transfer and cooling in gas turbines".* **VKI LS 1995-05.**

Jeong, J. & Hussain, F. 1995 On the identification of a vortex. *J. Fluid Mech.* **285,** 69-94.

Kalitzin, G. 1999 Application of v^2-f turbulence model to transonic flows. *AIAA-99-3780.*

Kalitzin, G. & Iaccarino G. 1999 Endwall heat transfer computations in a transonic turbine cascade. *XVII Congresso nazionale sulla transmissione del calore.* U.I.T, Ferrara, 30 June - 2 July.

Krist, S., Biedron, R. & Rumsey, C. 1998 CFL3D user's manual (Version 5.0). *NASA/TM-1998-208444.*

Spalart, P. R. & Allmaras, S. R. 1992 A one-equation turbulence model for aerodynamic flows. *AIAA 92-439.*